Last Glacial Maximum and Holocene Climate in CCSM3

BETTE L. OTTO-BLIESNER AND ESTHER C. BRADY

National Center for Atmospheric Research, Boulder, Colorado

GABRIEL CLAUZET

Department of Physical Oceanography, University of São Paulo, São Paulo, Brazil

ROBERT TOMAS, SAMUEL LEVIS, AND ZAV KOTHAVALA

National Center for Atmospheric Research, Boulder, Colorado

ABSTRACT

The climate sensitivity of the Community Climate System Model version 3 (CCSM3) is studied for two past climate forcings, the Last Glacial Maximum (LGM) and the mid-Holocene. The LGM, approximately 21 000 yr ago, is a glacial period with large changes in the greenhouse gases, sea level, and ice sheets. The mid-Holocene, approximately 6000 yr ago, occurred during the current interglacial with primary changes in the seasonal solar irradiance.

The LGM CCSM3 simulation has a global cooling of 4.5°C compared to preindustrial (PI) conditions with amplification of this cooling at high latitudes and over the continental ice sheets present at LGM. Tropical sea surface temperature (SST) cools by 1.7°C and tropical land temperature cools by 2.6°C on average. Simulations with the CCSM3 slab ocean model suggest that about half of the global cooling is explained by the reduced LGM concentration of atmospheric CO_2 (~50% of present-day concentrations). There is an increase in the Antarctic Circumpolar Current and Antarctic Bottom Water formation, and with increased ocean stratification, somewhat weaker and much shallower North Atlantic Deep Water. The mid-Holocene CCSM3 simulation has a global, annual cooling of less than 0.1°C compared to the PI simulation. Much larger and significant changes occur regionally and seasonally, including a more intense northern African summer monsoon, reduced Arctic sea ice in all months, and weaker ENSO variability.

1. Introduction

Global coupled climate models run for future scenarios of increasing atmospheric CO_2 concentrations give a range of responses of the global and regional climate change. Projected changes include amplification of the signal in the Arctic, possible weakening of the North Atlantic overturning circulation, changes in monsoons and the periodicity of drought, and modulation of tropical Pacific ENSO and its teleconnections, and these can vary significantly among models. The second phase of the Paleoclimate Modeling Intercomparison Project (PMIP-2) is coordinating simulations and data syntheses for the Last Glacial Maximum (LGM; 21 000 yr before present; 21 ka) and mid-Holocene (6000 yr before present; 6 ka) to contribute to the assessment of the ability of current climate models to simulate climate change. The responses of the climate system to LGM and Holocene forcings are large and should be simulated in the global coupled climate models being used for future assessments.

The important forcing for the LGM is not the direct effect of insolation changes, but the forcing resulting from the large changes in greenhouse gases, aerosols, ice sheets, sea level, and vegetation. Proxy data for the LGM indicate strong cooling at Northern Hemisphere (NH) high latitudes with a southward displacement and major reduction in area of the boreal forest (Bigelow et al. 2003) and cooling in Greenland of 21° ± 2°C (Dahl-Jensen et al. 1998). Sea ice in the North Atlantic was more extensive at LGM than at present but more sea-

Corresponding author address: Dr. Bette Otto-Bliesner, CCR/CGD, National Center for Atmospheric Research, P.O. Box 3000, Boulder, CO 80307-3000.
E-mail: ottobli@ucar.edu

sonally ice free than suggested by early reconstructions (Sarnthein et al. 2003; de Vernal et al. 2005). Southern high latitudes were also colder with cooling in eastern Antarctica of $9° \pm 2°C$ (Stenni et al. 2001) and large seasonal migration of sea ice around Antarctica (Gersonde et al. 2005). Ocean Drilling Program (ODP) core data for the LGM deep waters in the Atlantic indicate much colder and saltier waters than at present (Adkins et al. 2002).

The important forcing for the Holocene is the seasonal contrast of incoming solar radiation at the top of the atmosphere, which is well constrained (Berger 1978). This solar forcing is important for regional changes during the Holocene in the hydrologic cycle and global monsoons, expressed in surface changes of vegetation and lake levels, which can then modify the climate. Mid-Holocene proxy data indicate changes in vegetation and lake levels in the monsoon regions of Asia and northern Africa and expansion of boreal forest at the expense of tundra at mid- to high latitudes of the Northern Hemisphere (Prentice et al. 2000).

This paper discusses the climate predicted by the Community Climate System Model version 3 (CCSM3) for the Last Glacial Maximum and mid-Holocene. Forcings and boundary conditions follow the protocols established by the PMIP-2. Changes to the mean climate of the atmosphere, ocean, and sea ice and to interannual and decadal variability of the tropical Pacific region, the Arctic, and the Southern Ocean are described. Slab ocean simulations for the LGM are described to allow an evaluation of the sensitivity of CCSM3 to reduced atmospheric carbon dioxide and the relative role of CO_2 as compared to lowered sea level, continental ice sheets, the other trace gases, and ocean dynamics in explaining surface temperature changes.

2. Model description and forcings

The National Center for Atmospheric Research (NCAR) CCSM3 is a global, coupled ocean–atmosphere–sea ice–land surface climate model. Model details are given elsewhere in this special issue (Collins et al. 2006b). Briefly, the atmospheric model is the NCAR Community Atmospheric Model version 3 (CAM3) and is a three-dimensional primitive equation model solved with the spectral method in the horizontal and with 26 hybrid coordinate levels in the vertical (Collins et al. 2006a). For these paleoclimate simulations, the atmospheric resolution is T42 (an equivalent grid spacing of approximately 2.8° in latitude and longitude). The land model uses the same grid as the atmospheric model and includes a river routing scheme and specified but multiple land cover and plant functional types

within a grid cell (Dickinson et al. 2006). The ocean model is the NCAR implementation of the Parallel Ocean Program (POP), a three-dimensional primitive equation model in vertical z-coordinate (Gent et al. 2006). For these paleoclimate simulations, the ocean grid is 320×384 points with poles located in Greenland and Antarctica, and 40 levels extending to 5.5-km depth. The ocean horizontal resolution corresponds to a nominal grid spacing of approximately 1° in latitude and longitude with greater resolution in the Tropics and North Atlantic. The sea ice model is a dynamic–thermodynamic formulation, which includes a subgrid-scale ice thickness distribution and elastic–viscous–plastic rheology (Briegleb et al. 2004). The sea ice model uses the same horizontal grid and land mask as the ocean model.

The slab ocean configuration of CCSM3 includes a thermodynamic sea ice model coupled to the same atmosphere and land models as the fully coupled configuration. The ocean heat flux term is specified monthly and, as is often done for climate change simulations (LGM, Hewitt and Mitchell 1997; doubled CO_2, Kiehl et al. 2006), is based on the present-day (PD) calculation. It is adjusted to maintain the global mean of the present-day heat flux at the fewer ocean grid points with lower LGM sea level. Ocean mixed layer depths are specified geographically but not seasonally based on the data of Levitus (1982).

a. Radiative forcings

The coupled climate simulations for the LGM and mid-Holocene are compared to a preindustrial (PI) simulation. The PI simulation uses forcing appropriate for conditions before industrialization, ca. A.D. 1800, and follows the protocols established by PMIP-2 (http://www-lsce.cea.fr/pmip2/). The PI forcings and a comparison to a present-day simulation are described in detail elsewhere in this special issue (Otto-Bliesner et al. 2006).

Figure 1 shows the latitude–time distribution of solar radiation anomalies at the top of the atmosphere relative to the PI period for the LGM and the mid-Holocene simulations. The solar constant is set to 1365 $W m^{-2}$ in all three simulations. The largest absolute anomalies are found in the high latitudes. For the LGM, the NH summer high-latitude anomaly is about -12 $W m^{-2}$. For the mid-Holocene, high-latitude anomalies are much larger: 32 $W m^{-2}$ in the NH summer and 48 $W m^{-2}$ in the Southern Hemisphere (SH) spring. Annual mean anomalies are much smaller, less than 5 $W m^{-2}$, suggesting more modest annual impacts on climate.
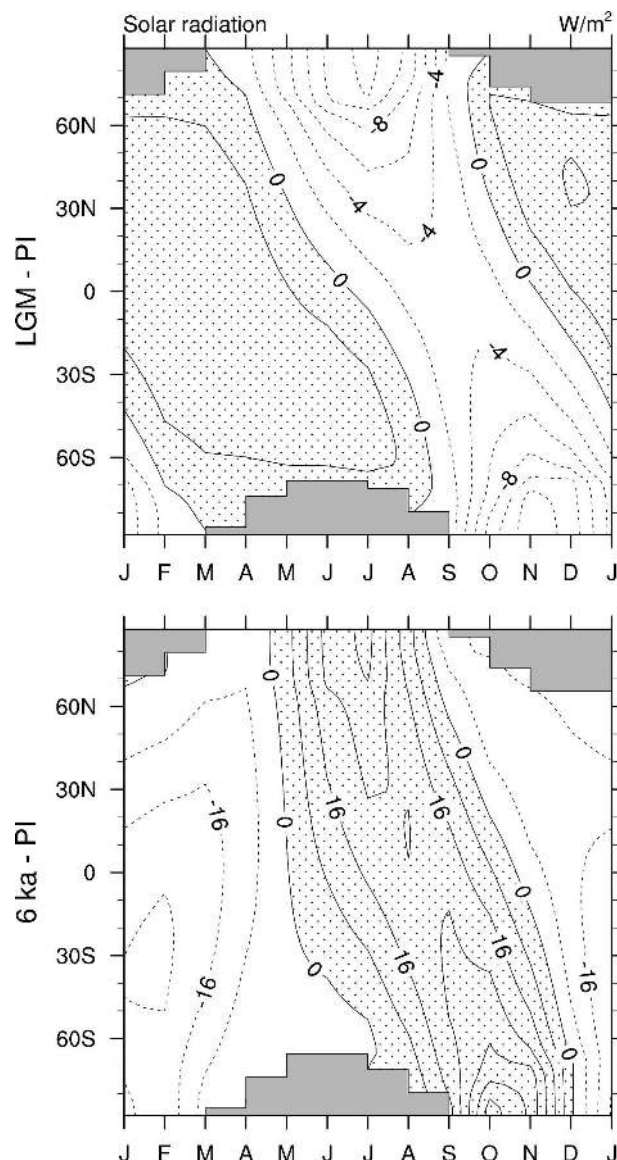
FIG. 1. The latitude–month distribution of solar radiation anomalies at the top of the atmosphere relative to PI for the LGM and the mid-Holocene simulations. The contour interval is 2 W m^{-2} for the LGM anomalies and 8 W m^{-2} for the mid-Holocene anomalies.

TABLE 1. Greenhouse gas concentrations for the PI, Holocene, and LGM simulations and estimates of the radiative forcing (W m^{-2}) relative to PI.

| | Greenhouse gas concentration | | | Radiative forcing | |
| | | | | LGM | 6 ka |
	LGM	6 ka	PI	W m^{-2}	W m^{-2}
CO_2	185 ppm	280 ppm	280 ppm	−2.22	0
CH_4	350 ppb	650 ppb	760 ppb	−0.28	−0.07
N_2O	200 ppb	270 ppb	270 ppb	−0.26	0

LGM simulation, concentrations of atmospheric carbon dioxide (CO_2), methane (CH_4), and nitrous oxide (N_2O) are decreased relative to the PI simulation, resulting in a total decrease in radiative forcing of the troposphere of 2.76 W m^{-2}. The majority of this change (2.22 W m^{-2}) results from a decrease in the amount of CO_2. In the mid-Holocene simulation, only the methane concentration differs from that used in the PI simulation, and it results in a 0.07 W m^{-2} decrease in radiative forcing.

b. LGM ice sheets, coastlines, and ocean bathymetry

The LGM ICE-5G reconstruction (Peltier 2004) is used for the continental ice sheet extent and topography in the LGM CCSM3 simulation. This new reconstruction differs from the version used in PMIP-1 (Peltier 1994), in both spatial extent and height of the ice sheets over Northern Hemisphere locations that were glaciated during the LGM. The Fennoscandian ice sheet does not extend as far eastward into northwestern Siberia. The Keewatin Dome west of Hudson Bay is 2–3 km higher in a broad area of central Canada in comparison to the ICE-4G reconstruction.

The coastline is also taken from the ICE-5G reconstruction and corresponds to a lowering of sea level of ~120 m. New land is exposed, most notably the land bridge between Asia and Alaska, through the Indonesian Archipelago, between Australia and New Guinea, and from France and the British Isles to Svalbard and the Arctic coastline of Eurasia. As suggested by PMIP-2, the present-day bathymetry is used in all LGM ocean regions except at relatively shallow sills (Strait of Gibraltar; the Denmark Strait) thought to be key to water mass formation; these sills are raised by ~120 m. This is an approximation that is different among the PMIP-2 modeling groups. Future sensitivity studies will consider the significance of these shallower sills on the LGM ocean simulation and the more detailed changes in paleobathymetry reconstructed by Peltier (2004).

Concentrations of the atmospheric greenhouse gases in the CCSM3 simulations are based on ice core measurements (Fluckiger et al. 1999; Dallenbach et al. 2000; Monnin et al. 2001) and differ in the PI, LGM, and mid-Holocene simulations (Table 1). Atmospheric aerosols are set at their preindustrial values in all three simulations. Also included in Table 1 are estimates of the radiative forcing on the troposphere using formulas from the 2001 Intergovernmental Panel on Climate Change (IPCC) report (Ramaswamy et al. 2001). In the

TABLE 2. Annual means and standard deviations (in parentheses) for the PI, Holocene, and LGM simulations.

	LGM	6 ka	Preindustrial
Global			
Surface temperature (°C)	8.99 (0.06)	13.44 (0.08)	13.52 (0.08)
Snow depth – land (water equiv cm)	18.85 (0.06)	9.37 (0.04)	9.49 (0.05)
Precipitation (mm day^{-1})	2.49 (0.01)	2.73 (0.01)	2.74 (0.01)
Precipitation − land (mm day^{-1})	1.77 (0.02)	2.04 (0.03)	2.02 (0.03)
Precipitation − ocean (mm day^{-1})	3.07 (0.01)	3.20 (0.01)	3.22 (0.01)
Precipitable water (mm)	18.11 (0.10)	21.98 (0.13)	22.19 (0.11)
Tropics (20°S–20°N)			
SST (°C)	24.86 (0.09)	26.37 (0.08)	26.58 (0.07)
Surface temperature − land (°C)	22.04 (0.11)	24.25 (0.11)	24.66 (0.11)
Extratropics (20°–90°)			
Southern Ocean SST (°C)	3.28 (0.07)	5.90 (0.06)	5.89 (0.09)
GIN Seas SST (°C)	0.66 (0.21)	4.49 (0.28)	4.32 (0.27)
Labrador Sea SST (°C)	−1.19 (0.08)	0.52 (0.27)	−0.17 (0.30)
SH sea ice area (10^6 km^2)	32.24 (0.42)	15.59 (0.46)	16.01 (0.53)
NH sea ice area (10^6 km^2)	10.36 (0.27)	12.88 (0.25)	13.33 (0.33)

3. Results

The mid-Holocene simulation is initialized from the PI simulation. This is also done for the LGM simulation except for the ocean. The LGM ocean is initialized by applying anomalies of the ocean three-dimensional potential temperature and salinity fields derived from an LGM simulation run with the Climate System Model version 1.4 (CSM1.4; Shin et al. 2003a) to the CCSM3 PI simulation. This approach allows a shorter spinup phase by starting with a previous LGM simulation that reached quasi-equilibrium and is one of the ocean spinup options proposed for participation in PMIP-2. The LGM and Holocene simulations are run for 300 yr. For many quantities, the simulations have reached quasi-equilibrium, although small trends still exist, particularly at Southern Hemisphere high latitudes and deep ocean. The mean climate results compare averages for the last 50 yr of the LGM and mid-Holocene simulations to the corresponding 50 yr of the PI simulation, except as noted. Significance testing of the atmospheric changes uses the Student's t test.

a. Global annual changes

The primary forcing change at 6 ka is the seasonal change of incoming solar radiation (Fig. 1). The net top-of-atmosphere annual change in this forcing is small, −1.1 W m^{-2} at the equator and 4.5 W m^{-2} at the poles compared to PI values. The simulated global, annual surface temperature is 13.4°C, a cooling of 0.1°C compared to the PI simulation (Table 2). Global, annual precipitation changes are small.

The LGM simulated surface climate is colder and drier than PI (Table 2). Simulated global, annual average surface temperature at LGM is 9.0°C, a cooling of 4.5°C from PI conditions. The LGM atmosphere is significantly drier with an 18% decrease in precipitable water and annual average precipitation is 2.49 mm day^{-1}, a decrease of 0.25 mm day^{-1} from PI. Snow depth doubles globally, and sea ice area doubles in the SH. In the NH, annual mean sea ice area decreases because lowered sea level reduces the area of the polar oceans.

Global, annual mean surface temperature simulated by the slab ocean version shows a cooling of 2.8°C for LGM CO_2 levels and a warming of 2.5°C for a doubling of CO_2, as compared to a present-day simulation. The slab and coupled CCSM3 simulations that include the reductions of the other atmospheric trace gases and the NH ice sheets at LGM give a cooling of 5.8°C compared to their present-day simulations and suggest that in CCSM3, atmospheric CO_2 concentration change explains about half of the global cooling at LGM.

b. Surface temperature

The mid-Holocene simulation has small but significant annual cooling over the tropical oceans and continents, generally less than 1°C associated with the reduced levels of methane and negative annual solar anomalies (Fig. 2). Greater annual cooling, in excess of 1°C in the Sahel, southern Arabia, and western India, is related to both winter cooling with negative solar anomalies and summer cooling with increased rainfall and cloudiness associated with an enhanced African–Asian monsoon. The Arctic Ocean and northern La-
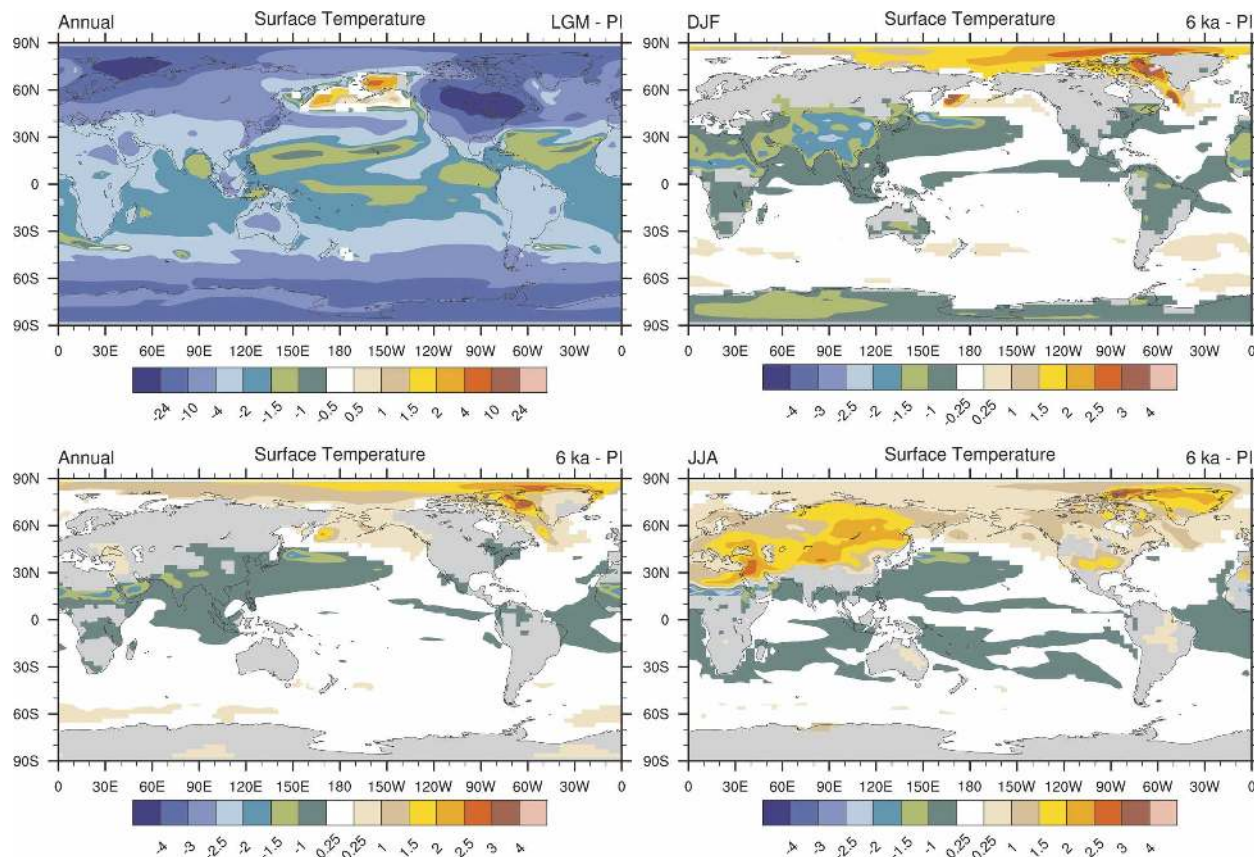
FIG. 2. CCSM3 surface temperature change (°C). (top left) Annual, LGM minus PI; (bottom left) annual, mid-Holocene minus PI; (top right) DJF, mid-Holocene minus PI simulation; and (bottom right) JJA, mid-Holocene minus PI. Only differences significant at 95% are shown.

brador Sea have annual warming in excess of 1°C and reduced sea ice.

Large positive solar anomalies occur in the NH in June–August (JJA) at 6 ka compared to PI (Fig. 1). These anomalies force significant summer warming over North America, Eurasia, and northern Africa (Fig. 2). Maximum warming, in excess of 2°C, occurs from 20°N over the Sahara extending to 65°N over central Russia and over northern Greenland. Weaker warming occurs over the SH continents with positive solar anomalies at these latitudes occurring 2–3 months later in the year.

Negative solar anomalies occur in both hemispheres in December–February (DJF) for the mid-Holocene as compared to PI (Fig. 1). The solar anomalies are largest in the SH, but because the SH is dominated by oceans and the NH contains the large continental masses of northern Africa and Eurasia, the largest cooling, up to 4°C, occurs over these regions between the equator and 40°N (Fig. 2). Significant cooling also occurs over eastern North America, Australia, southern Africa, South America, and Antarctica. The Arctic Ocean, Labrador

Sea, and North Pacific Ocean are up to 2°C warmer than PI because of the memory of the sea ice.

In the LGM simulation, greatest cooling occurs at high latitudes of both hemispheres, over the prescribed continental ice sheets of North America and Europe, and expanded sea ice in the north Atlantic and southern oceans (Fig. 2). In the Tropics (20°S–20°N), SSTs cool on average by 1.7°C and land temperatures cool on average by 2.6°C. The zonal gradient in the tropical Pacific relaxes, but only slightly, with cooling in the tropical Pacific warm pool of 1.6°C and in the cold tongue of 1.4°C. The Kuroshio and Gulf Stream currents simulated by CCSM3 are more zonal at LGM than PI and are located farther south in association with an equatorward shift of the subtropical gyres. Strong cooling in excess of 4°–8°C extends zonally across these ocean basins at these latitudes. Cooling over the subtropical oceans is smaller. Simulations with the CCSM3 slab ocean model indicate a feedback with subtropical low clouds such that for LGM, low clouds over the subtropical oceans decrease, thus reducing cooling, analogous to simulations for $2 \times CO_2$

when subtropical marine low clouds increase, reducing the warming.

Simulated surface temperatures are significantly warmer at LGM than PI in the North Pacific north of 50°N latitude and extending from east of the Kamchatka Peninsula to the Gulf of Alaska and northward into Alaska (Fig. 2). Greatest warming occurs in central Alaska (>4°C) and the western Bering Sea (>2°C). As in previous modeling studies with high Canadian ice sheets (CLIMAP Project Members 1981; Bromwich et al. 2004), the ICE-5G ice sheet in CCSM3 enhances the upper-air planetary wave structure in its vicinity with enhanced ridging over western Canada and enhanced troughs over the northwest Pacific and Labrador Sea–Greenland–eastern Atlantic (Fig. 3). At the surface, a large anticyclone dominates the flow over the ice sheet year-round, with maximum high pressure west of Hudson Bay. The Aleutian low deepens by 9 mb during DJF and 6 mb annually, and the North Pacific subpolar ocean gyre intensifies. Surface winds associated with the deepened Aleutian low are 30% stronger, enhancing advection of warmer air poleward into Alaska and the Gulf of Alaska.

These results contrast with results from CSM1, which using the lower ICE-4G ice sheet over North America had weak (2°C) cooling in this region. The role of the 2–3-km higher Keewatin Dome of the ICE-5G ice sheet is considered in a sensitivity simulation. In this sensitivity simulation, the ice sheet elevations are replaced with the lower ICE-4G heights in the region 50°–70°N, 85°–120°W. As compared to the ICE-5G LGM simulation, this sensitivity simulation has weaker 500-mb ridging over North America and reduced amplitude of the troughs over the North Pacific and North Atlantic (Fig. 3). At the surface, a weakened Aleutian low and reduced advection of warmer air poleward into Alaska and the Gulf of Alaska result in cooler temperatures and increased sea ice (Fig. 3). Compared to the PI simulation, the warming in the North Pacific is replaced by a cooling of 3°–3.5°C east of the Kamchatka Peninsula and a cooling of 0.5°–1.5°C over Alaska and the Gulf of Alaska.

LGM proxy indicators suggest modest cooling in the North Pacific region. Bigelow et al.'s (2003) analysis of pollen proxies in Alaska indicates colder conditions at LGM with a replacement of Alaskan forests by tundra. Only a few far North Pacific Ocean core reconstructions for the LGM have been published. Using planktonic foraminifera Mg/Ca, ODP Site 883 in the Bering Sea indicates LGM cooling of 0.6°C (Barker et al. 2005). An analysis of dinoflagellate cyst assemblages in core PAR87-A10 in the Gulf Alaska indicates that months of sea ice extent greater than 50% and winter
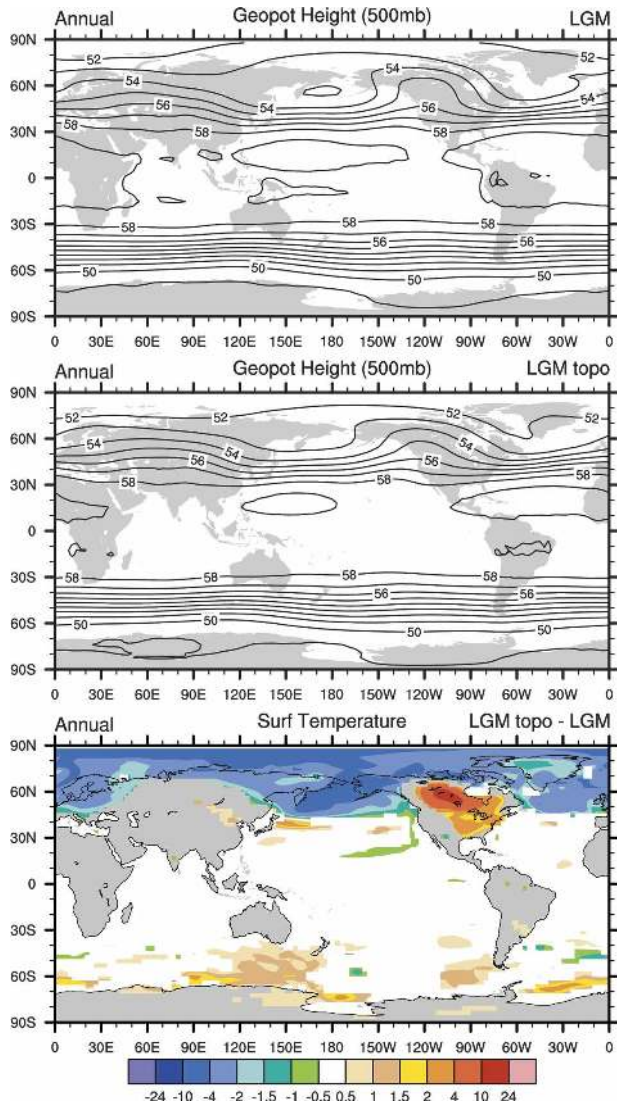

FIG. 3. Mean annual 500-mb geopotential height (hm) for (top) the LGM simulation and (middle) the LGM ice sheet topography sensitivity simulation. (bottom) Annual surface temperature difference (°C) with LGM ice sheet topography sensitivity simulation minus LGM simulation; only differences significant at 95% are shown.

sea surface temperature (SST) at LGM were similar to the present (de Vernal et al. 2005).

The role of ocean and sea ice dynamics on the response of CCSM3 to full LGM conditions may be assessed from Fig. 4. Ocean dynamics result in cooler Tropics, 1°C at the equator, and greater cooling in the southern than northern subtropics. The SH middle and high latitudes are significantly cooler in the coupled simulation with more extensive sea ice around Antarctica at LGM and greater low-cloud amounts to the north of the sea ice edge. The NH middle and high
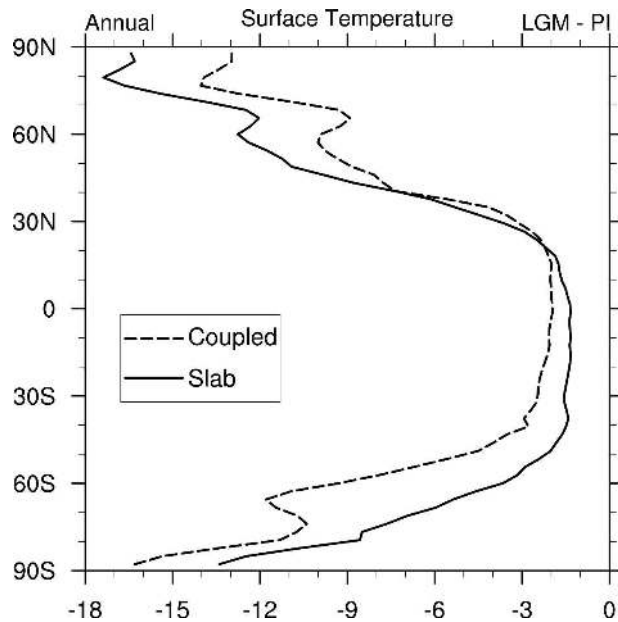
FIG. 4. Zonally averaged surface temperature changes (°C), LGM minus PI, simulated by the slab ocean (solid) and coupled ocean (dashed) versions of CCSM3.

latitudes are warmer in the coupled run with enhanced ocean heat transport, and reduced sea ice compared to the slab run in both the North Atlantic and Pacific Oceans. The bipolar response of CCSM3 to the inclusion of oceanic dynamics, with less cooling of surface temperatures at mid- and high northern latitudes and more cooling of surface temperatures at mid- and high southern latitudes, is similar to results from the Hadley Centre LGM simulations (Hewitt et al. 2003).

c. Sea ice

The simulated NH ice thickness and equatorward extent of ice in the mid-Holocene simulation is less than in the PI simulation (Fig. 5; also see Otto-Bliesner et al. 2006). Thickness differences range up to several meters and are collocated with the thickest ice for the Arctic Ocean and along the coast of Greenland. In contrast, the mid-Holocene and PI simulations have very similar SH ice thickness distributions. The seasonal cycles of the aggregate ice area are similar between the mid-Holocene and PI in both hemispheres.

The simulated LGM ice thickness and the equatorward extent of sea ice is considerably greater than the PI simulation. During the February–March season, sea ice thicknesses are 6–7 m over the Arctic Ocean, and extensive ice extends into the North Atlantic associated with the southward shift of the Gulf Stream in the LGM simulation. Maximum winter sea ice concentrations decrease up to 30% at LGM compared to PI over the

ocean from the Kamchatka Peninsula to the date line between 45° and 60°N in association with the North Pacific warming. In the SH, sea ice expands as far north as 45°S and has significant seasonal variation, especially in the Indian Ocean sector. Total ice area varies by a factor of ~2 between summer and winter in both hemispheres.

LGM extent of sea ice has been inferred from foraminifera paleotemperature estimates in the North Atlantic (Sarnthein et al. 2003) and diatoms and radiolarians for the Southern Ocean (Gersonde et al. 2005). The data suggest large seasonality in North Atlantic sea ice extent with the edge at 50°–60°N in winter and retreating far north, resulting in largely ice-free Nordic Seas during summer. CCSM3 results are in good agreement with the summer retreat but overestimate the winter extent in the western Atlantic at ~45°N. The data indicate that winter sea ice around Antarctica expands ~10° latitude to ~47°S in the Atlantic and Indian sectors and less so in the Pacific sector, to double area coverage from present to ~39 × 10^6 km². CCSM3 for LGM predicts a SH winter sea ice area of 40 × 10^6 km², the expansion in the Atlantic and Indian Oceans, and the asymmetric response of less sea ice in the Pacific sector. Southern Hemisphere summer sea ice extent is less well constrained by data; the data suggest greater seasonality than predicted by CCSM3 for LGM.

d. Precipitation

In the LGM simulation, precipitation decreases of up to 2 mm day^{-1} occur over the continental ice sheets (not shown). Decreases of precipitation also occur in the regions extending from the northeastern United States to northern Europe, eastward from Japan, and the northwest coast of Canada. In the Tropics, decreased precipitation occurs in the intertropical convergence zone (ITCZ), especially over the Atlantic and Indian Oceans and over South America, Oceania, and tropical Africa (Fig. 6).

Annual mean changes in precipitation simulated for the mid-Holocene reflect seasonal changes associated with the Milankovitch anomalies of solar insolation (Fig. 6). Drying at tropical latitudes of Africa is related to reduced precipitation in these regions in DJF. Increased annual precipitation in northern Africa and Saudi Arabia is associated with increased monsoonal precipitation during July–October. Warming of the North Atlantic as compared to the South Atlantic during August–October (ASO) (Fig. 6) results in a shift of the ITCZ northward and a longer monsoon season. Sea level pressure drops primarily north of 15°N with more than a 4-hPa decrease in the eastern Mediterra-
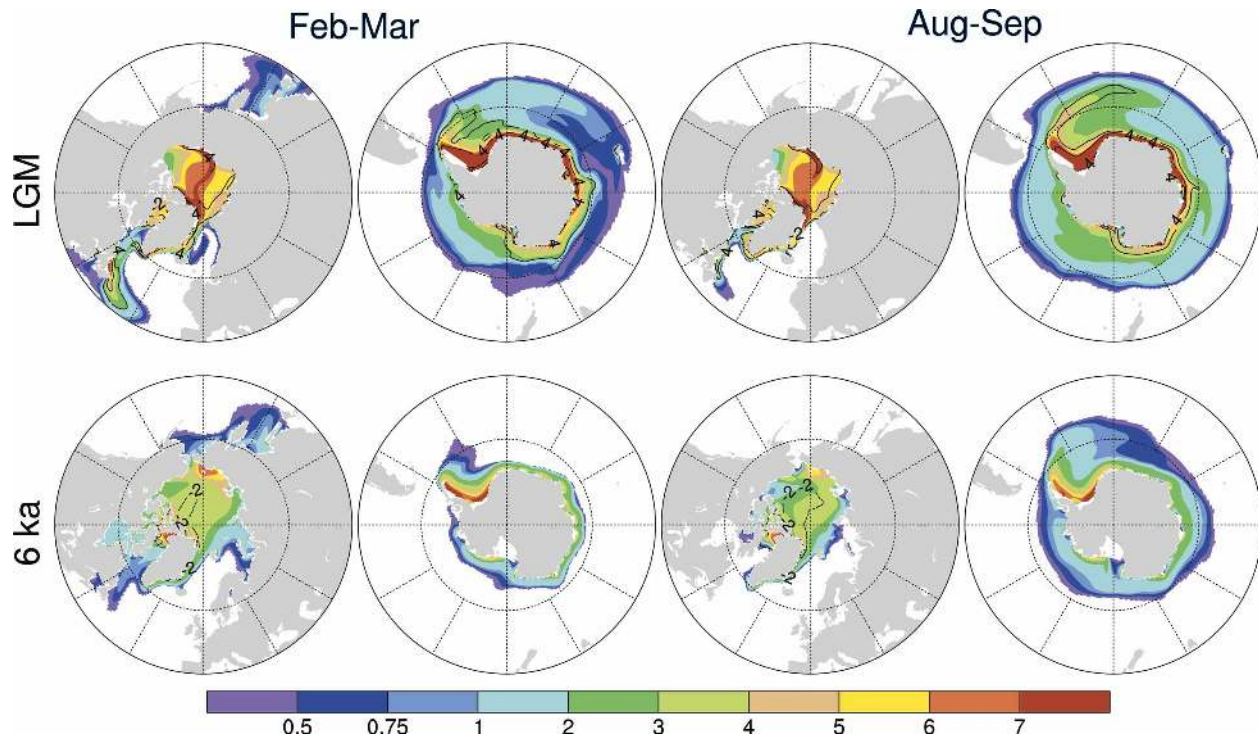
FIG. 5. CCSM3 ice thickness in meters (filled color contours) for February–March and August–September for the LGM and 6-ka simulations. Values less that 0.25 m are not colored. The differences from the PI simulation are shown as black line contours, negative values are dashed, the contour interval is 2 m, and the zero contour is omitted.

nean. Surface winds respond accordingly, with increases up to 6 m s^{-1} in westerly and southwesterly wind speeds over North Africa. These winds enhance the advection of moisture from the Atlantic Ocean to North Africa and the Arabian Peninsula. The combination of more net radiation and more soil moisture leads to an increase in both local recycling of precipitation and advection of moisture from the Atlantic. The pattern of Atlantic SST anomalies is similar although opposite in sign to those indicated for explaining Sahel drought in the latter decades of the twentieth century (Hoerling et al. 2006).

Simulated changes of the mid-Holocene North African monsoon are similar to those in the CCSM2 6-ka simulation (Levis et al. 2005) although with less northward shift than CCSM2 (Fig. 6). The reasons for this difference will be explored more fully with future sensitivity simulations. A 6-ka CSM1 simulation also gave a northward shift of African summer monsoon precipitation to 20°N but in CSM1 is associated with a shift of the ITCZ north rather than a latitudinal broadening of the monsoon precipitation as is the case in the CCSM2 and CCSM3 simulations (Fig. 6).

Terrestrial proxy records from the Holocene record a systematic northward extent of Sahelian vegetation belts, steppe, xerophytic woods/shrubs, and tropical dry

forest into the Sahara (Jolly et al. 1998), requiring increases in precipitation of 150–300 mm yr^{-1} from 18° to 30°N (Joussaume et al. 1999). CCSM3 predicts a northward shift in the monsoon extent over Africa with precipitation increases adequate to potentially support steppe vegetation growth to 20°N. Over the rest of northern Africa, CCSM3 remains too dry during the mid-Holocene. The CCSM3 Holocene simulation does not include predictive vegetation, which has been shown in some models to act as a positive feedback improving the simulation of Holocene precipitation over North Africa (Levis et al. 2005). At LGM, CCSM3 predicts drying and a reduced summer monsoon over tropical and northern Africa in agreement with proxy records of a desert extension farther south (Yan and Petit-Maire 1994; Prentice et al. 2000).

e. Ocean transports

There is a weak though significant reduction in the Antarctic Circumpolar Current (ACC) transport through the Drake Passage in the mid-Holocene simulation compared to PI (Table 3). Transports through the Florida and Bering Straits and Pacific Indonesian Throughflow are not significantly different between the mid-Holocene and PI simulations. The transport of the ACC is enhanced dramatically in the LGM simulation
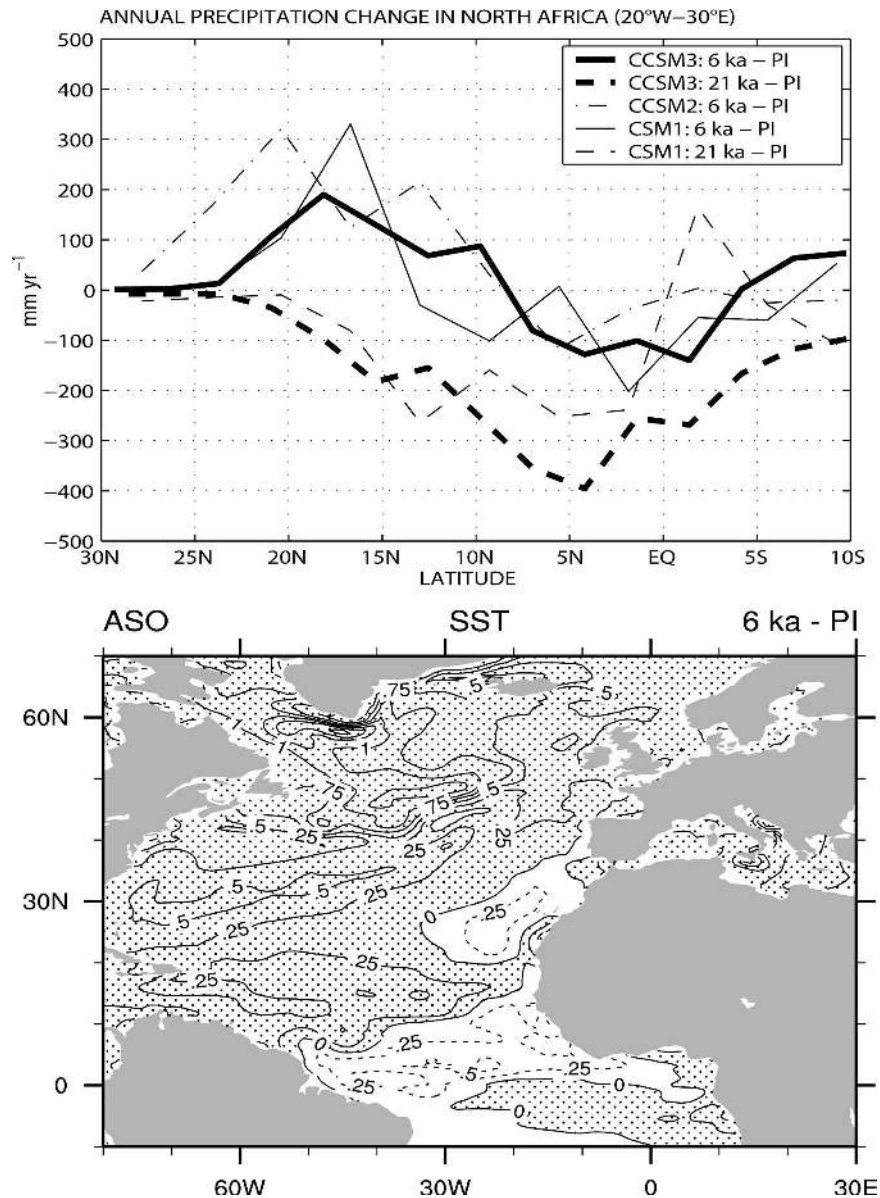
FIG. 6. (top) Annual precipitation change over North Africa in CCSM3, CCSM2, and CSM1 for the LGM and mid-Holocene. (bottom) Mean August–October (ASO) SST change (°C) over the Atlantic in the mid-Holocene simulation; contour interval is 0.25°C.

compared to PI (Table 3). This is due to both an increase in zonal wind stress in the Southern Ocean (Fig. 7) and an increase in Antarctic Bottom Water (AABW) formation with greater sea ice formation around Antarctica, which has been shown to be important for present ACC transport (Gent et al. 2001).

Simulated LGM wind stress is not stronger uniformly over the North Atlantic Ocean. A decrease in magnitude of the westerlies is notable north of 45°N; the westerlies shift southward in the LGM simulation. This southward shift of the westerlies is associated with a southward shift and weakening of the Icelandic low and the southward expansion of the ice pack edge. In the high-latitude North Atlantic, the winds are much stronger, especially in the Labrador and Greenland, Iceland, and Norwegian (GIN) Seas.

The LGM simulation shows a significant increase of ~6 Sv (1 Sv $\equiv 10^6$ m^3 s^{-1}; Table 3) in the volume transport through the Florida Straits (FS). This increase contradicts Lynch-Stieglitz et al. (1999), who suggested weaker FS transport based on a geostrophic calculation and proxy estimates of the cross-strait density gradient.

TABLE 3. Global annual mean and standard deviation (in parentheses) properties of the ocean for the PI, Holocene, and LGM simulations. The barotropic transport within key straits are computed over the last 100 yr of each simulation. Niño-3.4 statistics are computed over the last 150-yr periods of each simulation and smoothed with a 5-month boxcar filter.

	LGM	6 ka	Preindustrial
Ocean transports (Sv)			
Drake Passage	320.6 (3.8)	191.6 (3.4)	195.1 (3.2)
Indonesian Throughflow	−19.2 (1.1)	−18.5 (1.1)	−18.0 (1.5)
Florida Straits	34.5 (0.7)	28.2 (0.8)	28.3 (0.8)
Bering Strait	closed	0.87 (0.24)	0.93 (0.24)
Atlantic overturning (Sv)			
Max NADW	17.29 at 814 m	20.24 at 1022 m	21.00 at 1022 m
Max AABW (34°S)	−7.48 at 3250 m	−4.05 at 3750 m	−4.20 at 3750 m
Niño-3.4 statistics (°C)			
Standard deviation	0.59	0.66	0.83
Min	0.31	0.45	0.49
Max	0.77	0.85	1.06

The increase in the FS transport in the CCSM3 LGM simulation is largely attributable to the increase in the strength of the LGM wind stress (Fig. 7) and wind stress curl (not shown) across the Atlantic basin (Wunsch 2003). Compared to the PI simulation, the wind field of the LGM simulation causes a southward shift and intensification of the subtropical gyre. Increased wind stresses lead to enhanced mixed layer depths in the North Atlantic subtropical gyre, which is consistent with enhanced North Atlantic subtropical ventilation

rates inferred from proxy evidence (Slowey and Curry 1992).

f. Atlantic Ocean changes

Simulated mid-Holocene potential temperature and salinity changes in the Atlantic Ocean are small. The maximum mean meridional circulation (MOC) stream-function in the North Atlantic is only slightly weaker than in the PI simulation, but there is no difference in its depth and structure (Fig. 8; Table 3). The AABW
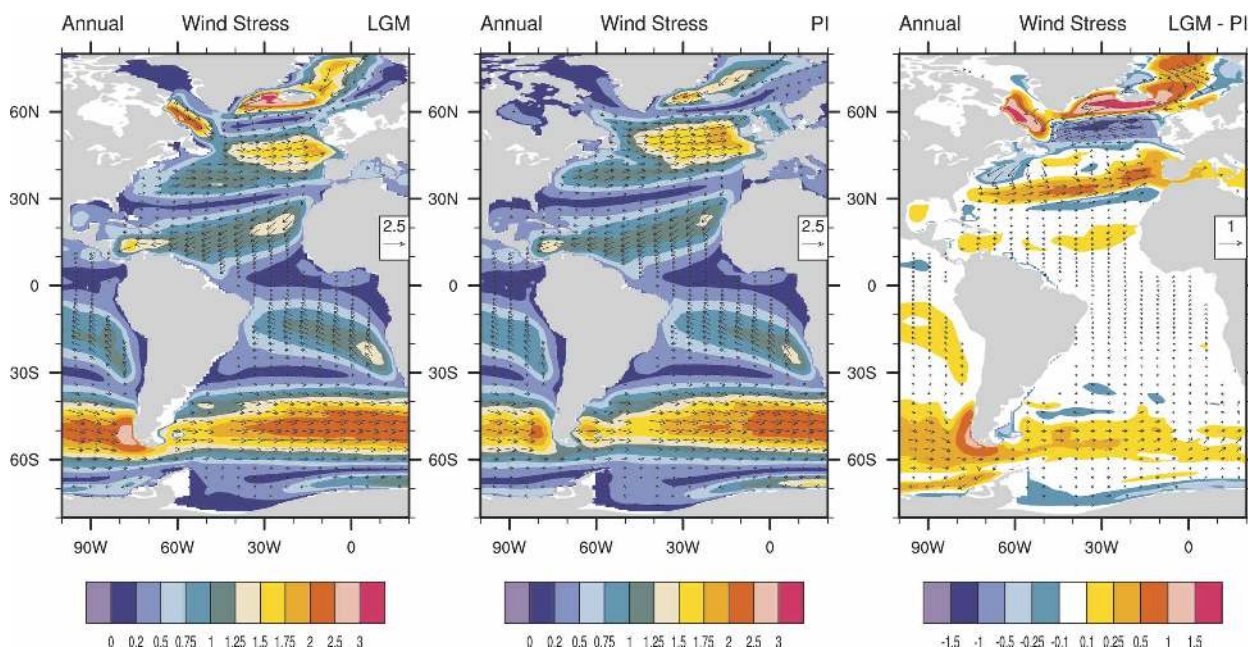

FIG. 7. CCSM3 annual wind stress vectors (dyn cm^{-2}) for the LGM and PI and change in wind stress, LGM minus PI, for 100°W–20°E.
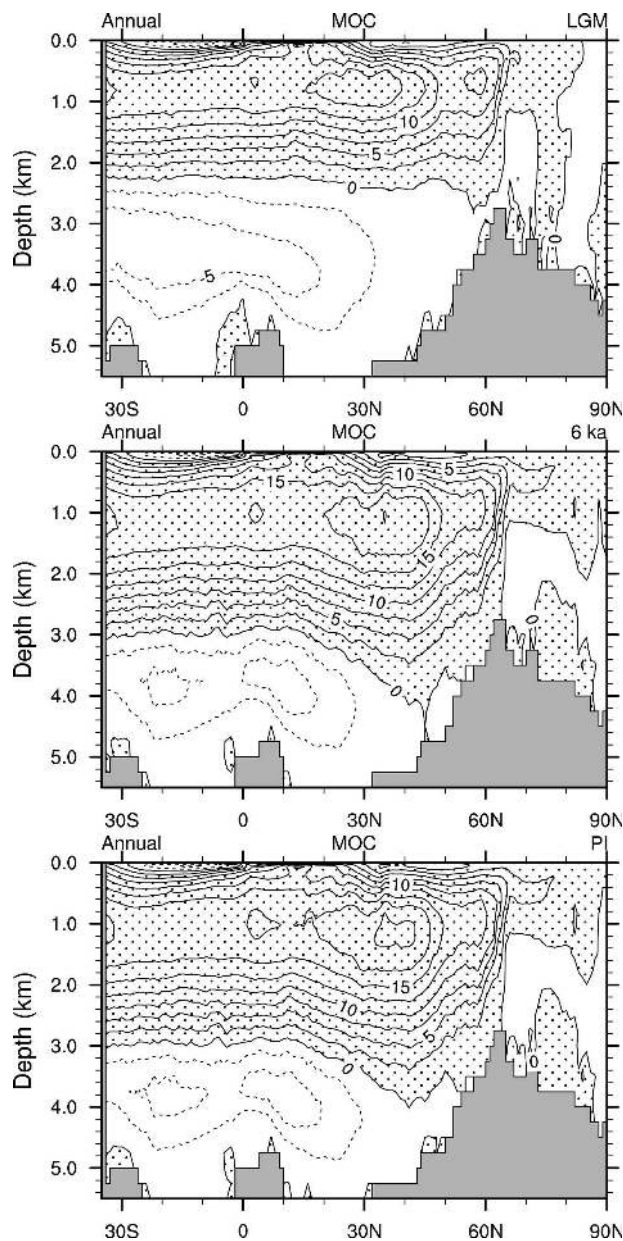
FIG. 8. Annual mean MOC by Eulerian mean flow in the Atlantic basin for the LGM, mid-Holocene, and PI simulations. Positive (clockwise) circulation is shown with solid lines, and negative (counterclockwise) circulation is given in dashed lines. Contour interval is 2.5 Sv.

streamfunction entering the South Atlantic at 34°S is similar in the mid-Holocene and PI simulations.

The LGM simulation is much colder and saltier than the PI simulation. In the Tropics and subtropics, basin-wide averages of annual mean SSTs predicted by CCSM3 for LGM fall within the range of proxy indicators (Fig. 9). In the South Atlantic, simulated SSTs agree with the proxy reconstructions except at higher

latitudes in the South Atlantic, where CCSM3 is colder than the Climate: Long-Range Investigation, Mapping, and Prediction (CLIMAP) Project as a result of considerable equatorward expansion of winter sea ice in this sector in CCSM3. In the North Atlantic, CCSM3-predicted and proxy-estimated SSTs for the tropical and subtropical North Atlantic are in agreement for LGM. CCSM3 predicts the sharpest gradient in SSTs 5° latitude equatorward of the proxy reconstructions, which is primarily a result of winter season SSTs in the model. CCSM3 is 1°–2°C too cold at high latitudes in the North Atlantic because predicted summer SSTs are too cold.

The global volume-averaged salinity in the LGM simulation is greater than the PI simulation. This increased salt (not shown) is distributed preferentially in the high-latitude regions and the deep and bottom water, with the most saline water found on the Antarctic shelf and at the bottom of the Arctic Ocean, suggesting enhanced brine rejection from increased sea ice formation. Brine rejection during sea ice formation, which is more vigorous and extensive in the LGM simulation, greatly enhances the salinity of the bottom waters in these basins.

Stratification of the CCSM3 PI Atlantic deep ocean is to a first order temperature driven similar to observed with warmer and saltier waters in the North Atlantic and colder and fresher waters in the South Atlantic (Fig. 10). Pore fluid measurements of chloride concentration and oxygen isotope composition at four Atlantic ODP sites from 55°N to 50°S (Adkins et al. 2002) find the LGM Atlantic deep ocean to be much colder and saltier than present, with the Southern Ocean deep ocean saltier than the North Atlantic. In agreement with these records, CCSM3 simulates relatively homogenous, very cold deep ocean temperatures in the Atlantic, and greatly increased deep ocean salinities with higher salinities in the Southern Ocean than at site 981. CCSM3 overestimates the increase in salinity except at the far southern site, Shona Rise.

In the Atlantic Ocean, the MOC associated with North Atlantic Deep Water (NADW) production is weaker and shallower in the LGM simulation than in the PI simulation (Fig. 8; Table 3). The LGM maximum MOC is 17.3 Sv at a depth of 814 m compared to 21.0 Sv at 1022 m in the PI simulation. There is a decrease in the export of NADW southward across 34°S at about 15.8 Sv compared to the PI value of 18.1 Sv. The zero streamfunction line, which delineates the surface water that has been converted to NADW, penetrates no deeper than ~2800 m as compared to 4000 m in the PI simulation. The transport of AABW, entering the South Atlantic at 34°S, is stronger and vertically more exten-
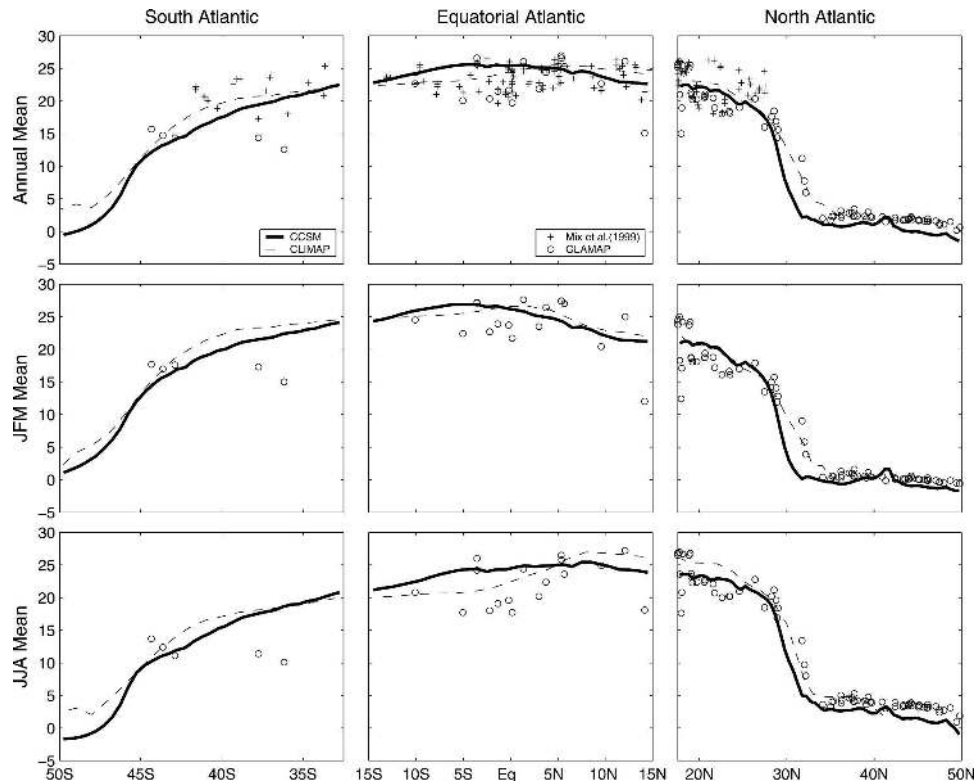
FIG. 9. Zonally averaged LGM sea surface temperatures (°C) predicted for the Atlantic basin by CCSM3 (solid line) as compared to the CLIMAP Project Members (1981) reconstruction (dashed line) and individual core estimates from Pflaumann et al.'s (2003) Glacial Ocean Mapping (GLAMAP) 2000 (circles) and Mix et al. (1999) (pluses).

sive with a shallower maximum in the LGM simulation of 7.5 Sv at 3250 m, compared to 4.2 Sv at 3750 m at PI.

Estimates of deep-ocean changes at the LGM have been derived from a variety of isotopic proxies including $\delta^{18}O$, $\delta^{13}C$, and Cd/Ca (Duplessy et al. 1980; Boyle and Keigwin 1982; Curry and Lohman 1982). These indicators have been interpreted as consistent with the NADW overturning being shallower and weaker than present and with waters at deep levels of the North Atlantic originating in the Southern Oceans. Newer paleonutrient tracers, neodymium and Zn/Ca (Rutberg et al. 2000; Marchitto et al. 2002), also point to reduced North Atlantic meridional overturning. Analysis of Pa/Th suggests that the strength was similar or slightly higher than at present (Yu et al. 1996) or reduced by no more than 30%–40% during the LGM (McManus et al. 2004). CCSM3 predicts a weaker and much shallower NADW with AABW dominating below 2.5 km as far north as 60°N in the Atlantic Ocean.

g. Extratropical modes of variability

The Arctic Oscillation (AO), defined as the first empirical orthogonal function of sea level pressure (SLP)

during boreal winter [December–March (DJFM)] from 20°–90°N, is the dominant observed pattern of nonseasonal variations of sea level pressure at middle and high latitudes in the Northern Hemisphere. For the PI simulation, AO explains 38% of the variance with sea level pressures of one sign circling the globe over the oceans at ~45°N and sea level pressures of the opposite sign centered over polar latitudes (Fig. 11). Similar to present observed correlations, during high AO years, northern Europe and Asia experience above-average temperatures and precipitation during the winter months, southern Europe has below-average precipitation, the Labrador Sea region is cooler and drier, and the southeastern United States is warmer. The AO in the CCSM3 PI simulation is discussed more completely in Otto-Bliesner et al. (2006).

For the mid-Holocene, the AO explains 37% of the variance. The patterns of variability are similar to PI. Correlations to surface temperature and precipitation are also similar to PI, except in southern Europe and the northern Mediterranean, where high AO years are associated with cooler temperatures.

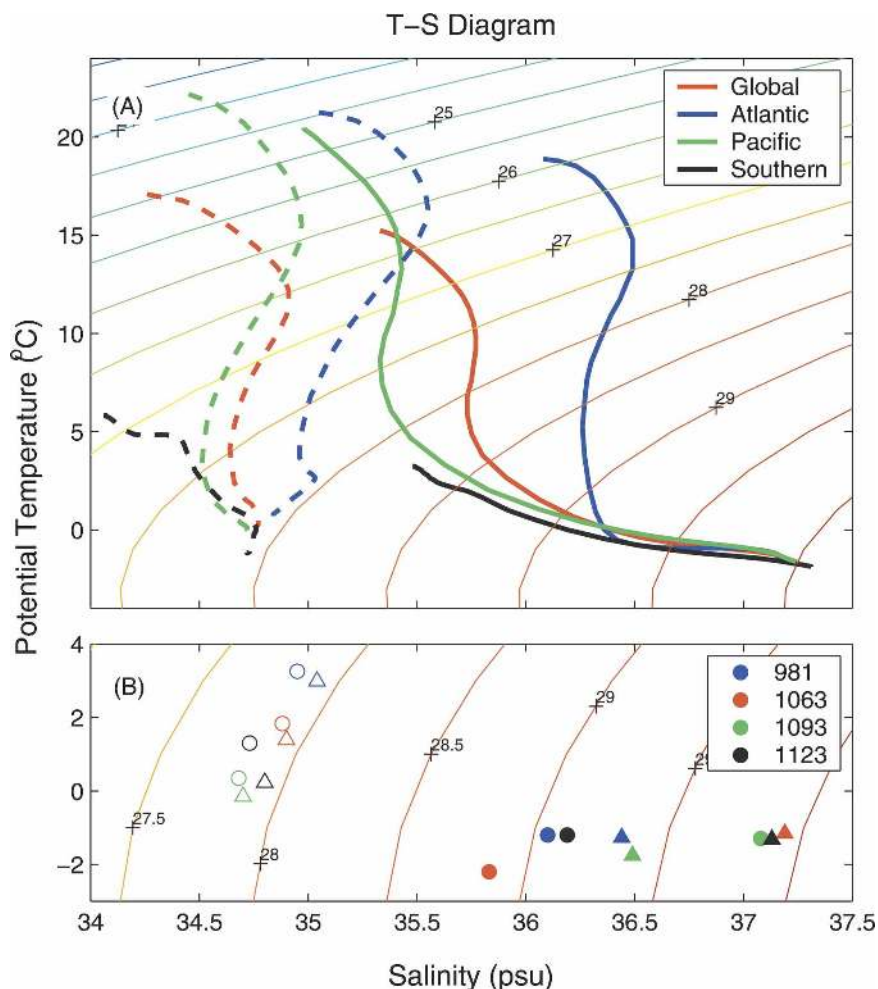At LGM, the ice sheets over North America and

T–S Diagram

FIG. 10. Temperature–salinity diagrams with (a) full-depth profiles averaged over the major ocean basins for the PI (dashed) and LGM (solid) simulations, and (b) deep ocean for modern observations (open circles), PI simulation (open triangles), LGM reconstruction (Adkins et al. 2002; solid circles), and LGM simulation (solid triangles) at four ODP sites: site 981 (blue) (Feni Drift; 55°N, 15°W; 2814 m), site 1063 (red) (Bermuda Rise; 34°N, 58°W; 4584 m), site 1093 (green) (Shona Rise; 50°S, 6°E; 3626 m), and site 1123 (black) (Chatham Rise; 42°S, 171°W; 3290 m). Contours indicate potential density (σ_θ) values in units of kg m^{-3}.

Europe and more snow and sea ice at high northern latitudes significantly affect sea level pressure variability. The AO explains only 27% of the variance, and the centers of variability are shifted and weakened. Sea level pressures are in phase over the Mediterranean and North Pacific west of the date line and out of phase with sea level pressure over northern Eurasia. Temperature and precipitation anomalies associated with AO variability are weaker (not shown).

The Antarctic Oscillation or Southern Annular Mode (SAM), defined here as the first EOF of SLP anomalies at 20°–90°S, represents the large-scale alternation of the atmospheric mass between the midlatitude and polar latitudes in the SH (Gong and Wang 1998). In the PI simulation, the SAM accounts for 36% of the total variance. Positive values of the SAM index are associated with negative SLP anomalies over Antarctica and positive anomalies at midlatitudes (Fig. 11). A center of minimum occurs near the Bellingshausen Sea region. At midlatitudes, enhanced SLP variability is located over the southern Pacific and Indian Oceans. Temperature and precipitation correlations are discussed in Otto-Bliesner et al. (2006).

The spatial patterns of the SAM for the LGM and mid-Holocene account for 39% and 35% of the variance, respectively. Sea level pressure patterns for all three simulations show a very similar structure, with a strong zonally symmetric component and an out-of-
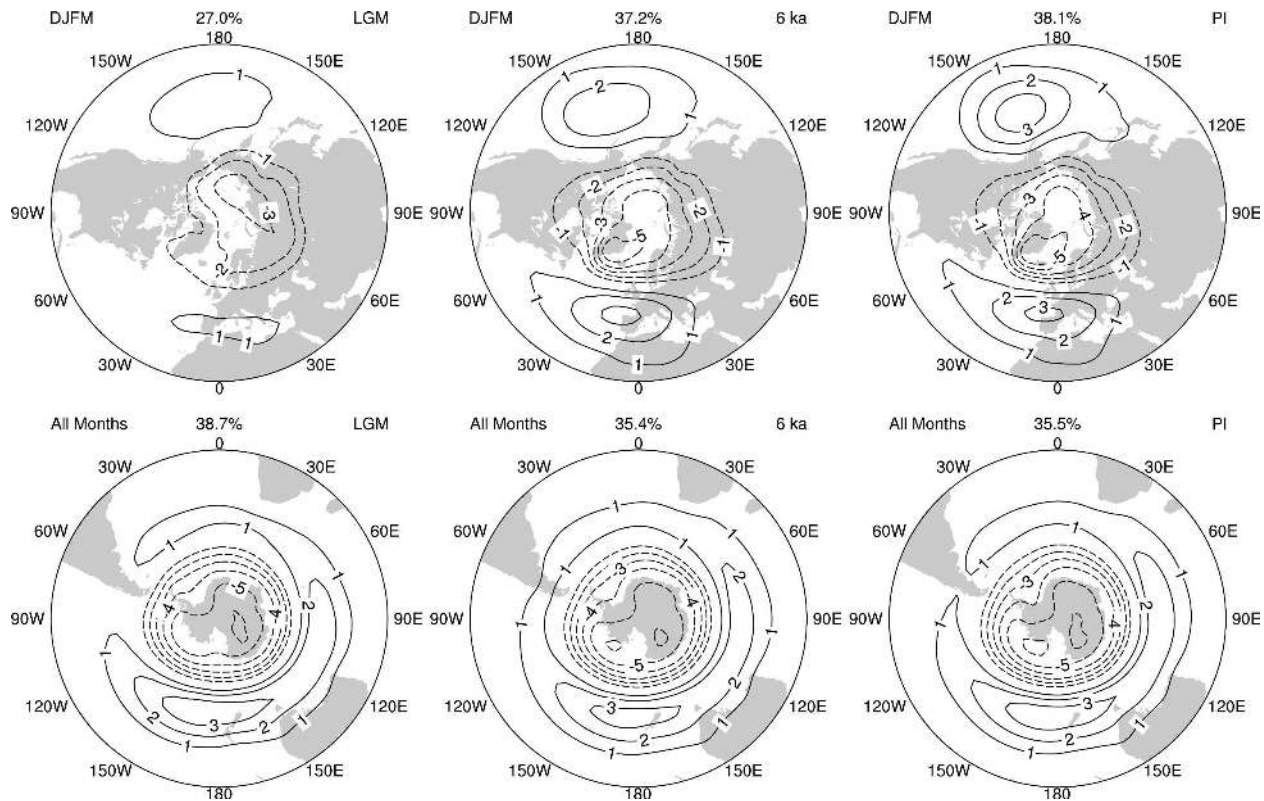
FIG. 11. (top) Arctic Oscillation and (bottom) Southern Annular Mode simulated for the LGM, mid-Holocene, and PI (units are hPa).

phase relationship between the Antarctic and midlatitudes at all longitudes. The patterns of temperature and precipitation correlation are similar in the mid-Holocene and PI simulations (not shown). The magnitudes of the temperature correlations are weaker at mid-Holocene. Correlations of surface temperature with the SAM at LGM are significantly weaker than PI.

h. Tropical Pacific interannual variability

The standard deviation of monthly SST anomalies averaged over the Niño-3.4 region (5°S–5°N, 170°–120°W) is presented as a measure of ENSO activity, as in the present-day CCSM3 simulations (Deser et al. 2006). The LGM and mid-Holocene CCSM3 simulations have weaker Niño-3.4 SST variability than the PI simulation (Table 3). While there is reduced Niño-3.4 variability during all months, the reduction is greatest in late boreal fall and winter seasons in both LGM and mid-Holocene simulations (Fig. 12). The mid-Holocene simulation suggests a weaker annual cycle of Niño-3.4 variability due to higher springtime variability relative to the winter maximum.

Coral records from Papua New Guinea have been interpreted to indicate that ENSO variability has ex-

isted for the past 130 000 yr but with reduced amplitude even during glacial periods, although a record for the Last Glacial Maximum at this site is absent because the coral reefs were above sea level in this region (Tudhope et al. 2001). Records from southern Ecuador also suggest weaker ENSO during the mid-Holocene (Rodbell et al. 1999). These ENSO indicators record changes in temperature or the hydrologic cycle and depend on the assumption of stationarity of the connection of the site to interannual variability of central and eastern Pacific equatorial SSTs.

4. Comparisons of CCSM3 LGM simulations to previous modeling results

Previous LGM coupled simulations used a variety of forcings and boundary conditions making strict comparisons difficult. Nonetheless, some comparisons are of interest. PMIP-2 has established protocols for the LGM and preindustrial simulations, which will allow more definitive comparisons to be done in the future

The global mean cooling in the LGM simulation is 4.5°C as compared to the PI simulation and 5.8°C as compared to a PD simulation. The CCSM3 global cool-
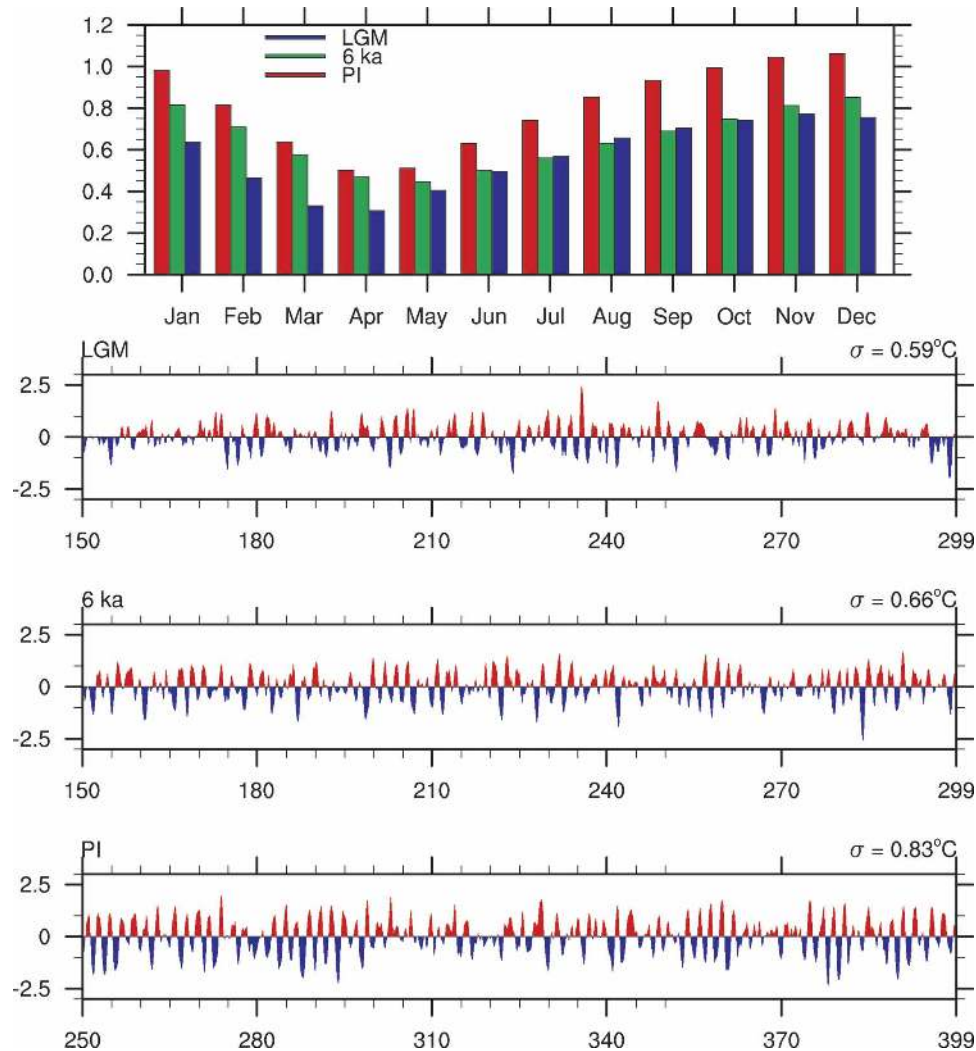
Fig. 12. (top) Monthly standard deviations and (bottom) time series of the Niño-3.4 SST anomalies
(°C) for the LGM, mid-Holocene, and PI simulations.

ing is 10% greater than simulated in the LGM CSM1 simulation (Shin et al. 2003a). Much of this additional cooling occurs at middle and high latitudes of both hemispheres. Global mean cooling in an LGM simulation with CSM1, as documented by Peltier and Solheim, is 9.0°C (Peltier and Solheim 2004). Their LGM simulation included aerosols in the atmospheric boundary layer 14 times larger than in their present-day simulation. These increased aerosols give an additional surface forcing of –3.9 W m^{-2} between their LGM and present-day simulations.

Tropical Pacific (20°S–20°N) SSTs in the CCSM3 LGM simulation cool by 1.7°C from the PI simulation and 2.6°C from a PD simulation. This cooling is comparable to that found in CSM1 although in CCSM3 it is more uniform across the Pacific, with SST decreases

from PI of 1.4°–1.8°C, except for SST cooling of 2.4°C in the far western tropical Pacific just offshore of the Indonesian Archipelago. CSM1 exhibited more zonal asymmetry in the LGM response in the tropical Pacific, with cooling of 1.8°C in the far eastern tropical Pacific (90°W) and cooling of 3.0°C in the warm pool (135°E) when compared to a present-day simulation (Otto-Bliesner et al. 2003). Modest cooling, up to 2.5°C, of tropical SSTs was also found in the MRI coupled simulations for LGM (Kitoh and Murakami 2002). Cooling in the Third Hadley Centre Coupled Ocean–Atmosphere GCM (HadCM3) at LGM showed significant zonal variation with cooling in the western and central tropical Pacific of 1°–1.5°C but cooling in excess of 3°–3.5°C in the eastern equatorial Pacific associated with enhanced upwelling (Rosenthal and Broccoli

2004). Strong cooling ($>-5°C$) was found in the CSM1 LGM simulation by Peltier and Solheim, and in the Geophysical Fluid Dynamics Laboratory (GFDL; Bush and Philander 1999) and Canadian Centre for Climate Modelling and Analysis (CCCMa) coupled LGM simulations. The stronger cooling found by Peltier and Solheim may be a result of warmer-than-observed tropical SSTs simulated in their present-day simulation (Otto-Bliesner and Brady 2001; Peltier and Solheim 2004).

The response of ENSO to cooling of the tropical Pacific at LGM is model dependent. Simulations with CSM1 (Otto-Bliesner et al. 2003; Peltier and Solheim 2004) have an enhancement of Niño-3.4 SST variability at LGM with reduced tropical teleconnections to rainfall variability in the western Pacific (Otto-Bliesner et al. 2003). An eigenmode analysis of ENSO in an intermediate complexity model driven by the mean CSM1.4 LGM background state (An et al. 2004) suggests that the presence of relatively colder water below the surface in the LGM and a weaker off-equatorial meridional temperature gradient in the Pacific are the most important factors leading to the enhanced growth of unstable ENSO modes in the CSM1. These effects are partially damped by the anomalous CSM1 LGM atmospheric conditions (winds and wind divergence). While the CCSM3 LGM simulation has similar Pacific Ocean changes, it has a weaker ENSO. This suggests that in CCSM3, the competing effect of LGM atmospheric changes is sufficient to damp ENSO growth rates. Timmerman et al. (2004) argue that the altered transient and stationary wave activity in the North Pacific by the LGM ice sheet may be important for regulating ENSO.

Peltier and Solheim (2002), using an LGM "centers of action" North Atlantic Oscillation (NAO) index, find an enhanced NAO in their simulation. Strong surface temperature variability over the NH continents is associated with their model glacial NAO. Rind et al. (2005) find changes in the pattern of AO in their ice age simulations with the GISS model. Their results show that changes in the eddy transport of sensible heat and high-latitude forcing dominate the AO response.

The NCAR CCSM3 and CSM1 LGM simulations both find an intensification of the ACC. One notable difference is that in CSM1, the westerly wind stress in the SH was found to both increase and shift poleward, whereas the westerlies in the CCSM3 LGM integration show a similar increase but no poleward shift. In CSM1, the ACC increased by about 50% at LGM. This is a much weaker response than the near doubling found in the CCSM3 LGM simulation. The larger response of the ACC with a similar wind stress change suggests that the CCSM3 may be more responsive to changes in thermohaline forcing than CSM1.

The CCSM3 results of a nearly 20% weaker and shallower MOC and of a stronger and more northward penetration of AABW at LGM are similar to what was found by Shin et al. (2003b) with CSM1. A noted difference is that the magnitude of the meridional overturning in the CCSM3 at LGM is 17 Sv compared to 21 Sv in CSM1. CCSM3 in the present-day simulation compares more favorably to modern observationally based estimates of NADW production (Bryan et al. 2006). CCSM3 also has a better present-day simulation of AABW in the Atlantic. In CSM1, AABW existed only below 4 km in the Atlantic basin and was underestimated in magnitude.

Other coupled model simulations of LGM show widely varying responses of the Atlantic meridional overturning. The Hadley Centre model (HadCM3) has an increase in both NADW and AABW at LGM, but with only minimal changes in the depth of these cells (Hewitt et al. 2003). The North Atlantic cell extends to 2.5 km in both LGM and the present. The HadCM3 LGM North Atlantic cell shifts southward in association with the expansion of Arctic sea ice. The Meteorological Research Institute (MRI) Coupled GCM version 1 (CGCM1) shows an increase of the North Atlantic MOC from 24 Sv at present to 30 Sv at LGM, with the LGM cell extending to the ocean bottom poleward of 40°N. In contrast, the CCCMa coupled simulation simulates an LGM overturning circulation in the North Atlantic that is 65% less than in their control and is restricted to latitudes poleward of 30°N. A reversed circulation occupies the Atlantic over its entire depth south of 30°N. They attribute this dramatic weakening to increased river runoff from the Amazon and Mississippi as well as an increase of precipitation-minus-evaporation over the North Atlantic.

5. Summary

In this paper, we describe the sensitivity of CCSM3 to the glacial forcings of the Last Glacial Maximum and the interglacial forcings of the mid-Holocene. The forcings changed for the LGM are reduced atmospheric greenhouse gases, a 2–3-km ice sheet over North America and northern Europe, lowered sea level resulting in new land areas, and small Milankovitch anomalies in solar radiation. The reduced LGM levels of atmospheric CO_2 are 66% of preindustrial levels and 55% of present levels in CCSM3. The forcings changed in the mid-Holocene are a small reduction in atmospheric methane and large changes in seasonal anomalies of solar radiation associated with Milankovitch orbital variations. As prescribed by PMIP-2, the comparisons are made to the climate simulated for preindustrial

conditions of ca. A.D. 1800. The sensitivity of CCSM3 to PI forcing changes as compared to present day is discussed in Otto-Bliesner et al. (2006).

The LGM CCSM3 simulation has a global cooling of 4.5°C compared to PI conditions with amplification of this cooling at high latitudes and over the continental ice sheets present at LGM. Tropical SSTs cool by 1.7°C and tropical land temperatures cool by 2.6°C on average. Note that this cooling is relative to PI conditions. Tropical SSTs cool by 2.6°C compared to the corresponding present-day simulation, suggesting that the calibration of proxy records requires clear identification of what time period "core-top" represents. Associated with these colder temperatures, the atmosphere is much drier with significantly less precipitable water. The LGM deep ocean is much colder and saltier than present. Compared to the PI simulation in which the deep ocean density stratification is to a first order temperature driven, the LGM ocean simulation has greater density stratification of deep waters due to increasing salinity. The increase in salinity in the LGM deep ocean is related to brine rejection associated with sea ice formation. The LGM simulation also has an increase in the Antarctic Circumpolar Current and Antarctic Bottom Water formation, increased ocean stratification, and weaker and shallower North Atlantic Deep Water.

CCSM3 slab ocean simulations suggest a symmetric but opposite sign of the surface temperature response to halving versus doubling atmospheric CO_2. This is true for both zonally averaged and regional temperature changes. The largest temperature changes in these slab ocean simulations forced by atmospheric CO_2 changes alone occur at high latitudes, that is, polar amplification associated with positive feedbacks of snow and ice. The smallest temperature changes occur over the subtropical oceans and are correlated with a negative feedback of low clouds in CCSM3. Ocean dynamics are also shown to be important in controlling the LGM temperature response to the changed forcings, warming NH middle and high latitudes, and cooling SH middle and high latitudes.

The mid-Holocene CCSM3 simulation has a global, annual cooling of less than 0.1°C compared to the PI simulation. Much larger and significant changes occur regionally and seasonally. Positive solar anomalies during July–September (JAS) at mid-Holocene force a more intense summer monsoon over northern Africa, which is further enhanced by a positive soil albedo–precipitation feedback in CCSM3. Positive solar anomalies in the Arctic during the summer months result in less and thinner sea ice in CCSM3. The simulated warming during summer of the Arctic persists through the winter months. NH sea ice thickness, and to a lesser

extent, sea ice concentration, are reduced year-round in the mid-Holocene simulation as compared to the PI simulation. ENSO variability, as measured by the Niño-3.4 standard deviation, is weaker in the mid-Holocene simulation and exhibits a noticeably weaker annual cycle.

The roles of vegetation and dust are still poorly constrained, especially for the LGM, but will be critical to include in future simulations to estimate their feedbacks. Estimates of LGM dust deposition rates indicate regional increases (Mahowald et al. 1999), which could significantly alter the magnitude and patterns of cooling in the Tropics with ramifications for simulated ENSO variability. The CCSM3 simulated warming in the North Pacific at LGM with the new ICE-5G ice sheet reconstruction differs from previous modeling results with the lower ICE-4G sheet in North America but agrees with previous GCM simulations with the higher CLIMAP ice sheet reconstruction (Kutzbach and Guetter 1986). An LGM sensitivity simulation with CCSM3 indicates that changes in surface temperature and winds in the North Pacific sector are sensitive to the height of the ice sheet over Canada. Isotopes will be included in future simulations to more directly compare to proxy records of LGM and mid-Holocene climate.

REFERENCES

Adkins, J. F., K. McIntyre, and D. P. Schrag, 2002: The salinity, temperature, and $\delta^{18}O$ of the glacial deep ocean. *Science,* **298,** 1769–1773.

An, S.-I., A. Timmermann, L. Bejarano, F.-F. Jin, F. Justino, Z. Liu, and A. W. Tudhope, 2004: Modeling evidence for enhanced El Niño–Southern Oscillation amplitude during the Last Glacial Maximum. *Paleoceanography,* **19,** 4009, doi:10.1029/2004PA001020.

Barker, S., I. Cacho, H. Benway, and K. Tachikawa, 2005: Planktonic foraminiferal Mg/Ca as a proxy for past oceanic temperatures: A methodological overview and data compilation for the Last Glacial Maximum. *Quat. Sci. Rev.,* **24,** 821–834.

Berger, A. L., 1978: Long-term variations of caloric insolation re-

sulting from the earth's orbital elements. *Quat. Res., 9,* 139–167.

Bigelow, N. H., and Coauthors, 2003: Climate change and Arctic ecosystems: 1. Vegetation changes north of 55°N between the last glacial maximum, mid-Holocene, and present. *J. Geophys. Res., 108,* 8170, doi:10.1029/2002JD002558.

Boyle, E. A., and L. Keigwin, 1982: Deep circulation of the North Atlantic over the last 200, 000 years: Geochemical evidence. *Science, 218,* 784–787.

Briegleb, B. P., C. M. Bitz, E. C. Hunke, W. H. Lipscomb, M. M. Holland, J. L. Schramm, and R. E. Moritz, 2004: Scientific description of the sea ice component in the Community Climate System Model, Version 3. NCAR Tech. Note NCAR/TN-463+STR, 70 pp.

Bromwich, D. H., E. R. Toracinta, H. Wei, R. J. Oglesby, J. L. Fastook, and T. H. Hughes, 2004: Polar MM5 simulations of the winter climate of the Laurentide Ice Sheet. *J. Climate, 17,* 3415–3433.

Bryan, F. O., G. Danabasoglu, N. Nakashiki, Y. Yoshida, D.-H. Kim, J. Tsutsui, and S. C. Doney, 2006: Response of North Atlantic thermohaline circulation and ventilation to increasing carbon dioxide in CCSM3. *J. Climate, 19,* 2382–2397.

Bush, A. B. G., and S. G. H. Philander, 1999: The climate of the Last Glacial Maximum: Results from a coupled atmosphere-ocean general circulation model. *J. Geophys. Res., 104,* 24 509–24 525.

CLIMAP Project Members, 1981: Seasonal reconstructions of the earth's surface at the Last Glacial Maximum. Tech. Rep. MC-36, Geological Society of America, 18 pp.

Collins, W. D., and Coauthors, 2006a: The formulation and atmospheric simulation of the Community Atmosphere Model version 3 (CAM3). *J. Climate, 19,* 2144–2161.

——, and Coauthors, 2006b: The Community Climate System Model version 3 (CCSM3). *J. Climate, 19,* 2122–2143.

Curry, W. B., and Lohman, 1982: Carbon isotope changes in benthic foraminifera from the western South Atlantic reconstruction of glacial abyssal circulation patterns. *Quat. Res., 18,* 218–235.

Dahl-Jensen, D., K. Mosegaard, N. Gundestrup, G. D. Clow, S. Johnsen, A. W. Hansen, and N. Balling, 1998: Past temperature directly from the Greenland Ice Sheet. *Science, 282,* 268–271.

Dallenbach, A., T. Blunier, J. Fluckiger, B. Stauffer, J. Chappellaz, and D. Raynaud, 2000: Changes in the atmospheric CH$_4$ gradient between Greenland and Antarctica during the Last Glacial and the transition to the Holocene. *Geophys. Res. Lett., 27,* 1005–1008.

Deser, C., A. Capotondi, R. Saravanan, and A. Phillips, 2006: Tropical Pacific and Atlantic climate variability in CCSM3. *J. Climate, 19,* 2451–2481.

de Vernal, A., and Coauthors, 2005: Reconstruction of sea-surface conditions at middle to high latitudes of the Northern Hemisphere during the Last Glacial Maximum (LGM) based on dinoflagellate cyst assemblages. *Quat. Sci. Rev., 24,* 897–924.

Dickinson, R. E., K. W. Oleson, G. B. Bonan, F. Hoffman, P. Thorton, M. Vertenstein, Z.-L. Yang, and X. Zeng, 2006: The Community Land Model and its climate statistics as a component of the Community Climate System Model. *J. Climate, 19,* 2302–2324.

Duplessy, J. C., J. Moyes, and C. Pujol, 1980: Deep water formation in the North Atlantic ocean during the last ice age. *Nature, 286,* 476–482.

Fluckiger, J., A. Dallenbach, T. Blunier, B. Stauffer, T. F. Stocker, D. Raynaud, and J.-M. Barnola, 1999: Variations in atmospheric N$_2$O concentration during abrupt climatic changes. *Science, 285,* 227–230.

Gent, P. R., W. G. Large, and F. O. Bryan, 2001: What sets the mean transport through the Drake Passage? *J. Geophys. Res., 106,* 2693–2712.

——, F. O. Bryan, G. Danabasoglu, K. Lindsay, D. Tsumune, M. W. Hecht, and S. C. Doney, 2006: Ocean chlorofluorocarbon and heat uptake during the twentieth century in the CCSM3. *J. Climate, 19,* 2366–2381.

Gersonde, R., X. Crosta, A. Abelmann, and L. Armand, 2005: Sea-surface temperature and sea ice distribution of the Southern Ocean at the EPILOG Last Glacial Maximum—A circum-Antarctic view based on siliceous microfossil records. *Quat. Sci. Rev., 24,* 869–896.

Gong, D.-Y., and S.-W. Wang, 1998: Antarctic oscillation: Concept and applications. *Chinese Sci. Bull., 43,* 734–738.

Hewitt, C. D., and J. F. B. Mitchell, 1997: Radiative forcing and response of a GCM to ice age boundary conditions: Cloud feedback and climate sensitivity. *Climate Dyn., 13,* 821–834.

——, R. J. Stouffer, A. J. Broccoli, J. F. B. Mitchell, and P. J. Valdes, 2003: The effect of ocean dynamics in a coupled GCM simulation of the Last Glacial Maximum. *Climate Dyn., 20,* 203–218.

Hoerling, M. P., J. W. Hurrell, and A. Phillips, 2006: Detection and attribution of twentieth-century northern and southern African rainfall change. *J. Climate,* in press.

Jolly, D., and Coauthors, 1998: Biome reconstruction from pollen and plant macrofossil data for Africa and the Arabian Peninsula at 0 and 6000 years. *J. Biogeogr., 25,* 1007–1027.

Joussaume, S., and Coauthors, 1999: Monsoon changes for 6000 years ago: Results of 18 simulations from the Paleoclimate Modeling Intercomparison Project (PMIP). *Geophys. Res. Lett., 26,* 859–862.

Kiehl, J. T., C. A. Shields, J. J. Hack, and W. D. Collins, 2006: The climate sensitivity of the Community Climate System Model version 3 (CCSM3). *J. Climate, 19,* 2584–2596.

Kitoh, A., and S. Murakami, 2002: Tropical Pacific climate at the mid-Holocene and the Last Glacial Maximum simulated by a coupled ocean-atmosphere general model. *Paleoceanography, 17,* 1047, doi:10.1029/2001PA000724.

Kutzbach, J. E., and P. J. Guetter, 1986: The influence of changing orbital parameters and surface boundary conditions on climate simulations for the past 18 000 years. *J. Atmos. Sci., 43,* 1726–1759.

Levis, S., G. B. Bonan, and C. Bonfils, 2005: Soil feedback drives the mid-Holocene North African monsoon northward in fully coupled CCSM2 simulations with a dynamic vegetation model. *Climate Dyn., 23,* 791–802.

Levitus, S., 1982: *Climatological Atlas of the World Ocean.* NOAA Prof. Paper, 13, 173 pp. and 17 microfiche.

Lynch-Stieglitz, J., W. B. Curry, and N. Slowey, 1999: Weaker Gulf Stream in the Florida Straits during the Last Glacial Maximum. *Nature, 402,* 644–648.

Mahowald, N., K. Kohfeld, M. Hannson, Y. Balkanski, S. P. Harrison, I. C. Prentice, M. Schulz, and H. Rohde, 1999: Dust sources and deposition during the Last Glacial Maximum and current climate: A comparison of model results with paleodata from ice cores and marine sediments. *J. Geophys. Res., 104,* 15 859–15 916.

Marchitto, T. N. J., D. W. Oppo, and W. B. Curry, 2002: Paired benthic foraminiferal Cd/Ca and Zn/Ca evidence for a greatly increased presence of Southern Ocean Water in the glacial

North Atlantic. *Paleoceanography,* **17,** 1038, doi:10.1029/2000PA000598.

McManus, J. F., R. Francois, J.-M. Gherardi, L. Keigwin, and S. Brown-Leger, 2004: Collapse and rapid resumption of Atlantic meridional circulation linked to deglacial climate changes. *Nature,* **428,** 834–837.

Mix, A. C., A. E. Morey, N. G. Pisias, and S. W. Hostetler, 1999: Foraminiferal faunal estimates of paleotemperature: Circumventing the no-analog problem yields cool ice age tropics. *Paleoceanography,* **14,** 350–359.

Monnin, E., A. Indermuhle, A. Dallenbach, J. Fluckiger, B. Stauffer, T. F. Stocker, D. Raynaud, and J. M. Barnola, 2001: Atmospheric CO_2 concentrations over the last glacial termination. *Science,* **291,** 112–114.

Otto-Bliesner, B. L., and E. C. Brady, 2001: Tropical Pacific variability in the NCAR Community Climate System Model. *J. Climate,* **14,** 3587–3607.

——, ——, S. Shin, Z. Liu, and C. Shields, 2003: Modeling El Niño and its teleconnections during the last glacial-interglacial cycle. *Geophys. Res. Lett.,* **30,** 2198, doi:10.1029/2003GL018553.

——, R. Tomas, E. C. Brady, C. Ammann, Z. Kothavala, and G. Clauzet, 2006: Climate sensitivity of moderate- and low-resolution versions of CCSM3 to preindustrial forcings. *J. Climate,* **19,** 2567–2583.

Peltier, W. R., 1994: Ice age paleotopography. *Science,* **265,** 195–201.

——, 2004: Global glacial isostasy and the surface of the ice-age Earth: The ICE-5G (VM2) model and GRACE. *Annu. Rev. Earth Planet. Sci.,* **32,** 111–149.

——, and L. P. Solheim, 2002: Dynamics of the ice age earth: Solid mechanics and fluid mechanics. *J. Phys. IV,* **12,** 85–104.

——, and ——, 2004: The climate of the Earth at Last Glacial Maximum: Statistical equilibrium state and a mode of internal variability. *Quat. Sci. Rev.,* **23,** 335–357.

Pflaumann, U., and Coauthors, 2003: Glacial North Atlantic: Sea-surface conditions reconstructed by GLAMAP 2000. *Paleoceanography,* **18,** 1065, doi:10.1029/2002PA000774.

Prentice, I. C., D. Jolly, and Biome 6000 Participants, 2000: Mid-Holocene and glacial-maximum vegetation geography of the northern continents and Africa. *J. Biogeogr.,* **27,** 507–519.

Ramaswamy, V., and Coauthors, 2001: Radiative forcing of climate change. *Climate Change 2001: The Scientific Basis,* J. T. Houghton et al., Eds., Cambridge University Press, 349–416.

Rind, D., J. Perlwitz, P. Lonergan, and J. Lerner, 2005: AO/NAO response to climate change: 2. Relative importance of low- and high-latitude temperature changes. *J. Geophys. Res.,* **110,** D12108, doi:10.1029/2004JD005686.

Rodbell, D. T., G. O. Seltzer, D. M. Anderson, M. B. Abbott, D. B. Enfield, and J. H. Newman, 1999: An ~15,000-year record of El Niño-driven alluviation in southwestern Ecuador. *Science,* **283,** 516–520.

Rosenthal, Y., and A. J. Broccoli, 2004: In search of paleo-ENSO. *Science,* **304,** 219–221.

Rutberg, R. L., S. R. Hemming, and S. L. Goldstein, 2000: Reduced North Atlantic deep water flux to the glacial Southern Ocean inferred from neodymium isotope ratios. *Nature,* **405,** 935–938.

Sarnthein, M., U. Pflaumann, and M. Weinelt, 2003: Past extent of sea ice in the northern North Atlantic inferred from foraminiferal paleotemperature estimates. *Paleoceanography,* **18,** 1047, doi:10.1029/2002PA000771.

Shin, S. I., Z. Liu, B. L. Otto-Bliesner, E. C. Brady, J. E. Kutzbach, and S. P. Harrison, 2003a: A simulation of the Last Glacial Maximum Climate using the NCAR CSM. *Climate Dyn.,* **20,** 127–151.

——, ——, ——, J. E. Kutzbach, and S. J. Vavrus, 2003b: Southern ocean sea-ice control of the glacial North Atlantic thermohaline circulation. *Geophys. Res. Lett.,* **30,** 1096, doi:10.1029/2002GL015513.

Slowey, N., and W. B. Curry, 1992: Enhanced ventilation of the North Atlantic subtropical gyre thermocline during the last glaciation. *Nature,* **358,** 665–668.

Stenni, B., V. Masson-Delmotte, S. Johnsen, J. Jouzel, A. Longinelli, E. Monnin, R. Rothlisberger, and E. Selmo, 2001: An oceanic cold reversal during the last deglaciation. *Science,* **293,** 2074–2077.

Timmerman, A., F. Justino, H. Goosse, and F.-F. Jin, 2004: Surface temperature control in the North and tropical Pacific during the last glacial period. *Climate Dyn.,* **23,** 353–370.

Tudhope, A. W., and Coauthors, 2001: Variability in the El Niño-Southern Oscillation through a glacial-interglacial cycle. *Science,* **291,** 1511–1517.

Wunsch, C., 2003: Determining paleoceanographic circulations, with emphasis on the Last Glacial Maximu. *Quat. Sci. Rev.,* **22,** 371–385.

Yan, Z., and N. Petit-Maire, 1994: The last 140 ka in the Afro-Asian arid/semi-arid transitional zone. *Palaeogeogr., Palaeoclimatol. Palaeoecol.,* **110,** 217–233.

Yu, E.-F., R. Francois, and P. Bacon, 1996: Similar rates of modern and last-glacial ocean thermohaline circulation inferred from radiochemical data. *Nature,* **379,** 689–694.